DYNAMIC STUDY OF FLEXIBLE SENSORS TO REDUCE MOTION ARTIFACTS

A Dissertation
Presented to
The Academic Faculty

by

Nathan A. Rodeheaver

In Partial Fulfillment
of the Requirements for the Degree
Master of Science in Mechanical Engineering in the
School of George W. Woodruff School of Mechanical Engineering

Georgia Institute of Technology

May 2021

DYNAMIC STUDY OF FLEXIBLE SENSORS TO REDUCE MOTION ARTIFACTS

Approved by:

Dr. W. Hong Yeo, Advisor
School of Mechanical Engineering
Georgia Institute of Technology

Dr. Rudolph Gleason
School of Mechanical Engineering
Georgia Institute of Technology

Dr. Suresh Sitaraman
School of Mechanical Engineering
Georgia Institute of Technology

Date Approved: April 14, 2021

To the God and Creator of a dynamic world.

“In Him we live and move and have our being”

Acts 17:28

ACKNOWLEDGEMENTS

I would like to thank the following people who have contributed in many ways throughout my life and specifically during the preparation of this thesis:

- My advisor, Dr. W. Hong Yeo, for his willingness to take me on as a graduate student despite my lack of knowledge of wearable electronics at the time. His knowledge and desire for quality have challenged me to continue improving. His attention to detail has taught me the value of clear communication, especially using figures to tell a story.
- The members of my research group who share what they are researching each week, it has provided new perspectives for problem solving. I want to specifically thank Dr. Yun-Soung Kim, Dr. Hojoong Kim, Dr. Hyoryoung Lim, Dr. Young-Tae Kwon, Shinjae Kwon, Robert Herbert, Musa Mahmood, Jongsu Kim, Nathan Zavanelli, Jihoon Kim, Carl Demolder, Sung Hoon Lee, Bu Li, and Ricardo Goldoni who have taught me technical skills, reviewed my papers, shared code, and taken my samples out of the oven when I wasn't there.
- To my parents, John and Renata, who raised me in a loving home. You taught me the value of integrity and hard work. Thank you for your support, encouragement, and persistence that I finish my degree.
- To my wife, Anna, you are the love of my life, my encourager, and the woman who makes me a better man! Thank you for all your support despite long hours at the lab and my grumpiness when another experiment fails.
- To my daughters, Leah, Abigail and Rebekah, your joy for life and curiosity encourages me to see the world in new ways. I also promise to make the treehouse now.

TABLE OF CONTENTS

ACKNOWLEDGEMENTS **iv**

LIST OF TABLES **vii**

LIST OF FIGURES **viii**

SUMMARY **ix**

CHAPTER 1. INTRODUCTION **1**

CHAPTER 2. BACKGROUND **3**

2.1 ECG Measurement **3**

2.2 Motion Artifact Definition **5**

2.3 A Review of ECG Devices and Current Limitations **7**

2.3.1 ECG Device Categories 7

2.3.2 Limitations and Solutions 8

CHAPTER 3. SYSTEM OVERVIEW **11**

CHAPTER 4. MATERIALS AND METHODS **14**

4.1 Materials **14**

4.1.1 SIS Assembly 14

4.1.2 Elastomer Substrate Fabrication 15

4.1.3 Electrode Fabrication 16

4.2 Strain Isolation **17**

4.2.1 Contact Impedance 17

4.2.2 Skin Strain Model 19

4.2.3 Strain Layer Material Characterization 21

4.2.4 Strain Layer Development 22

4.3 Finite Element Analysis **24**

4.4 Signal Processing **24**

CHAPTER 5. RESULTS AND DISCUSSION **27**

5.1 Material Results **27**

5.1.1 Adhesion 27

5.1.2 Breathability 28

5.1.3 Strain Reduction 30

5.2 ECG Results of SIS **31**

5.2.1 Comparison with Identical Electrodes 31

5.2.2 Comparison with Commercial Device 33

5.2.3 Validation of Long-term Monitoring 36

CHAPTER 6. CONCLUSION AND FUTURE WORK **38**

6.1 Conclusion **38**

6.2 Future Work **38**

REFERENCES **39**

LIST OF TABLES

Table 2.1. Effects of Relative Motion on an ECG Device 7

Table 2.2 Comparison of wearable ECG monitoring systems. 10

LIST OF FIGURES

Figure 2.1 ECG plot with diagram of the human heart[7, 8] 4

Figure 2.2 Equivalent circuit representation[12] 6

Figure 2.3 ECG devices by category 8

Figure 3.1 Overview of the SIS 12

Figure 4.1 SIS assembly steps..... 14

Figure 4.2 Breathable substrate fabrication 16

Figure 4.3 Electrode fabrication..... 17

Figure 4.4 Sources of impedance change..... 18

Figure 4.5 Skin strain model 20

Figure 4.6 Strain layer material characterization 22

Figure 4.7 Schematic of strain isolation layer..... 23

Figure 4.8 FEA mesh and loading conditions..... 24

Figure 4.9 ECG signal filtering and SNR calculation..... 26

Figure 5.1 Results of adhesion peel test..... 28

Figure 5.2 Results of water vapor transmission test with breathable elastomer 30

Figure 5.3 FEA and experimental results of axial strain test 31

Figure 5.4 Results of jogging test with SIS compared to no strain isolation..... 32

Figure 5.5 Results of simultaneous testing of SIS and commercial device 35

Figure 5.6 Results of 8-hour ECG measurement with multiple activities 37

SUMMARY

The field of wearable electronics is changing healthcare and increasing possibilities for human-machine interfaces. Soft electronics stretch with the skin to monitor long-term heart rate trends or direct the motion of smart prosthetics. The capabilities are only as good as the signal quality. A significant challenge for these devices is that by their very definition – wearable – these flexible sensors suffer from motion artifacts not previously found when measured in a stationary setting. This thesis investigates three significant sources of motion artifacts for flexible sensors: relative motion between sensor and signal source, the unique challenges of skin strain, and change in contact impedance. Relative motion is not a unique problem for wearable electronics. Still, human tissue's elastic nature means that most body-mounted sensors undergo more relative motion than on a comparable rigid machine. Device design is analyzed showing a small form factor, and lightweight designs reduce device motion. Human skin is an unstable platform to mount devices. Skin strain causes device movement and changes the biopotential during measurement. Experimental examples show material and design solutions to increase adhesion, reduce strain within the device, and maintain breathability for long-term recordings. Flexible sensors measuring biopotential are susceptible to changes in contact impedance. Skin strain and vibrations create motion artifacts that can mimic or disrupt many biosignals, making them hard to filter out. A prototype device is presented that uses a strain isolating layer to reduce skin strain at the electrode, which stabilizes contact impedance and reduces motion artifacts. Experimental data from the device compensating for these three sources of motion artifacts is presented for quantitative comparison.

CHAPTER 1. INTRODUCTION

Wearable electronics are everywhere and are estimated to make up an $104 billion market by 2027[1]. Forbes estimates that with the advancement in wearable technology, there will be a $200 billion savings in healthcare costs over the next 25 years[2]. Medical tests that once required expensive clinical equipment only found in a medical facility can now be done by the patient at home with a portable device. The COVID-19 quarantine of this past year, 2020, has forced the world to think differently about virtual healthcare. Expanding healthcare monitoring beyond the clinic can provide the general population with more routine access to medical advice. Using wearable electronics to collect data outside the clinic can also give medical providers access to better patient data as well. Instead of showing up to the doctor's office to measure weight blood pressure, we could wear a heart monitor the day before. This data can be wirelessly transferred securely to the doctor's portal, and a full heart health assessment can be made based on the hearts real-time response to various activities throughout the day. The electrocardiogram (ECG) and accelerometer data from multiple hours can provide better insight beyond the narrow time window most patients spend with their healthcare provider.

This is an optimistic view of the future, and to be sure, not all wearable electronics will make our lives happier and healthier. It is estimated that 1/3 of all fitness trackers are unused after just six months of being purchased, and very few popular devices are FDA approved for clinical level data[3]. To be worth the effort of wearing, these devices must solve a problem and add value for the user as well as the healthcare provider. For example, cardiovascular diseases affect 48% of the adult population in the United States and continue

to be the number one cause of death worldwide[4]. Portable, long-term, continuous monitoring of ECG is urgently needed to detect the onset of various arrhythmias that can happen anytime during daily activities. Many ambulatory ECG devices have been developed to provide smaller form factors than the gold-standard Holter monitor. Collecting high-quality data outside the clinical setting remains challenging due to motion artifacts (MA). In fact, most wearable devices rely on relatively simple electronics to measure optical or electrical measurements from the skin[5] and are thereby easily susceptible to motion artifacts. A motion artifact is the temporary change in measured voltage caused by the movement of the sensor and/or body where the sensor is located.

This goal of this thesis is to investigate the main causes of motion artifacts and develop a wireless ECG device with improved signal quality by eliminating these sources of signal noise. A background review of ECG measurement, wearable ECG devices, and current limitations is followed by a system overview of the prototype device developed during this research. Next, the testing methods and materials are presented. Next, the results of analytical calculations, comparison with commercial devices, and demonstration of long-term ECG recording are discussed. Finally, a review of the contributions and potential for future study conclude the thesis.

CHAPTER 2. BACKGROUND

2.1 ECG Measurement

The electrocardiogram, sometimes abbreviated EKG due to the German spelling, is the measurement of the heart's electrical activity. ECG measurement began around 1902 and was pioneered by Dr. Willem Einthoven who developed the PQRST annotation we use today[6]. The heart is a muscle, and muscle contraction and relaxation is caused by ionic exchange within the muscle fibers. The resulting electrical activity travels through the body and is measured on the skin surface using electrodes. The time varying amplitude of the voltage at a given location is the superposition of all the muscle activity in the body at that instant in time. The signal from a particular muscle fiber gets weaker as it travels through the body, so most ECG electrodes are placed strategically on the chest to pick up a clear, dominant signal from the heart (Figure 2.1B). Figure 2.1A shows the ECG waveform plotted as electrical amplitude versus time. This represents the sequence with which different muscle fibers in the heart contract or relax, moving from left to right to form the PQRST sequence. This plot corresponds to the areas labeled in Figure 2.1C, where generally, the orange lines indicate muscle contraction, and the white lines indicate relaxation[7]. The P wave is the firing of the SA node, followed by the PR interval which is a delay of electrical impulse at the AV node that allows blood to fill the appropriate chambers. Next the QRS complex is the contraction of both ventricles to pump blood out of the heart. The R peak is what is generally referred to as the heartbeat because it is the most dominant period with the largest amount of muscle contraction. Following this is the

ST segment when the ventricles begin repolarization. The T wave is a result of this repolarization as the heart is prepared for another cycle.

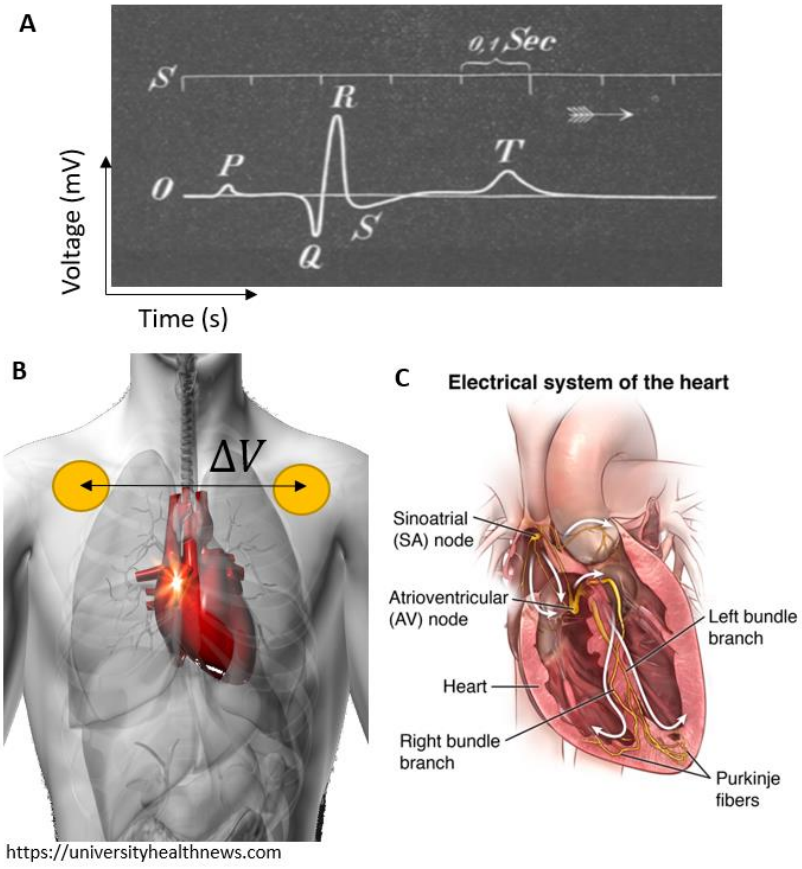

Figure 2.1 ECG plot with diagram of the human heart[7, 8]

A more detailed description of heart function is beyond the scope of this thesis. However, the sequence described above shows how a non-invasive ECG measurement can provide detail into the complex functions of the heart. One can also imagine that a signal this complex can only be relied upon for detailed measurements if it is very precise. The P and T waves are similar in size, and any disturbance of the overall electrical measurement can create noise that could mimic these small features. The most common of these disturbances is a motion artifact, which is defined in the next section.

2.2 Motion Artifact Definition

A motion artifact has been defined as

> "a phenomenon or feature not originally present or expected and caused by an interfering external agent, action, or process, as an unwanted feature in a microscopic specimen after fixation, in a digitally reproduced image, or in a digital audio recording"[9].

A brief search for the term will likely produce journal articles dealing with blurred X-ray images or CT scans, and a blurry picture is a good image to have in mind. Imagine taking a picture of an athlete. In this case, reflected light is the signal and it is coming from the signal source, the athlete. The camera, or more specifically, the optical sensor inside the camera is the sensor. When the camera and the athlete are both stationary the picture is clear, this is the first case. The second case is when the camera is stationary, but the athlete is moving, resulting in a blurry picture. The third case is when the athlete is stationary, but the camera is moving, also resulting in a blurry picture. A fourth case is also possible, when both the athlete and the camera are moving together exactly. This is hard to do by walking but is very common when riding in a vehicle. The picture remains clear no matter how fast the vehicle is moving because there is no relative motion between the source and the sensor. The relative motion between the sensor and source of the signal is what created the blurry picture.

In the same way, relative motion between any sensor and the source of the signal being measured will cause a motion artifact. Because the ECG is an electrical signal, the entire setup can be modeled as an electrical system and is depicted in Figure 2.2. Any change to

the properties of the system will change the voltage being measured. For ECG signals, any relative motion that disturbs the signal while traveling from the heart to the device can be considered a motion artifact. The signal can be disturbed in different ways throughout the entire system. For example, walking creates a downward force on the skin and ECG device with every step, which causes temporary stretching of the skin and relative motion of the skin with the electrode. Together, these two disturbances change the half-cell potential of the skin as well as the contact impedance with the electrode, respectively[10]. Additionally, vibrations that originate from the leg can travel through the skin and jiggle the circuit or disrupt the electrode contact. These temporary changes in the measured voltage can have the same amplitude and frequency as the heart rate[11], making them difficult to distinguish from many physiological signals.

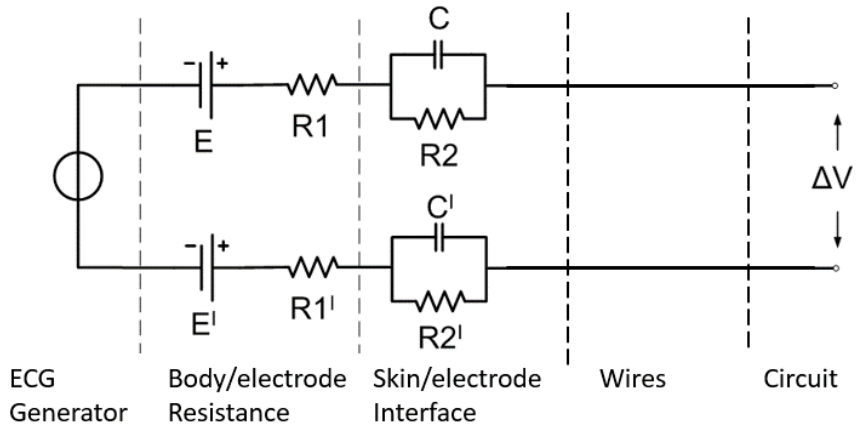

Figure 2.2 Equivalent circuit representation[12]

A list of changes to the system, ordered by the locations from Figure 2.2, is shown in Table 2.1. Examples of activities that cause this relative motion include, but are not limited to, walking, jogging, stretching, coughing, laughing, riding in an accelerating vehicle, etc. The consistent feature of these activities is that the activity introduces relative motion between the device and the heart, disturbing the signal. Some works include items such as

powerline interference and baseline drift[13] as motion artifacts because this type of noise is common in ambulatory ECG measurement, but they are not included in this study. Although motion is often involved, such as walking through an electromagnetic field that distorts the signal, the mechanism causing powerline interference is fundamentally different than the motion artifact caused by walking. Next, we will review how other ECG devices have performed.

Table 2.1. Effects of Relative Motion on an ECG Device

Area	Relative motion	Resulting change
Circuit	Strain, bending	Resistance Damage to components
Wires	Strain	Resistance
Skin/electrode	Strain	Resistance Skin contact Disconnection
Body/electrode	Strain, vibrations	Half-cell potential

2.3 A Review of ECG Devices and Current Limitations

2.3.1 ECG Device Categories

ECG devices developed and used over the past few decades include a wide range of designs and strategies. They can be arranged in four general categories shown in Figure 2.3. Starting clockwise from the top left is a clinical standard 12-lead ECG where the patient is usually seated or laying and connected with gel electrodes and wires. The top right is an ambulatory Holter monitor that also uses gel electrodes and wires, but the device is battery powered and capable of recording data for over 24 hours. Next, the bottom right is a patch device, often called a single lead, that uses adhesive gel electrodes. This device is capable of multi-day monitoring, but not usually continuous data, rather it is event triggered to only record when an irregular heartbeat is detected. Finally, on the bottom left

there is a fitness tracker. These often use straps around the chest or are only a wrist mounted device.

Figure 2.3 ECG devices by category

2.3.2 Limitations and Solutions

Further development of prototype and single lead devices has shown good results. The smaller size allows greater mobility. In addition to reducing size, many other techniques have been used to improve signal quality. Software algorithms and signal filtering are commonly used to improve signal quality, but are computationally expensive, especially

for long-term monitoring, and still only provide an estimate of the actual biosignal[14-17]. Filtering can also be done on any signal as a secondary improvement method but is incapable of improving the raw data. Another solution is to use pressurized tight straps to restrict device movement on the skin[18, 19]. However, this method causes severe discomfort and restriction of the user's activities. If a user loosens the strap pressure, the sensor loses the proper contact to the skin, resulting in signal degradation. Some devices use conductive gels to reduce impedance or strong adhesives to reduce movement, but this often creates skin rash after extended use or even skin breakdown when removed[20-24]. Recent studies have shown possible applications of dry, adhesive-free electrodes that make gentle lamination on the skin[25-27]. However, these still suffer from excessive MA caused by multiple wires, the rigidity of sensors, and the electrode's movement on the skin. Dry electrodes are especially sensitive to skin strain and vibration induced by body motion while walking, reaching, and performing other daily activities[5, 14, 28, 29].

One improvement in dry electrode design was the development of thin-film, open-mesh electrodes capable of stretching with the skin. Previous works have shown some reduction of MA using the mesh electrodes compared to rigid electrodes due to their conformal contact[30-34]. Others have shown the correlation between signal quality and electrode contact area[34-36]. This led to investigating the mechanisms causing changes to conformal contact and electrode contact area, showing that skin strain at the electrode is the main source of MA for dry electrodes. Although recently reported devices have used soft materials[37-41] or serpentine patterns[42-44], no prior work has shown the capability of a wearable device to significantly reduce MA caused by skin-electrode strain from external sources.

Table 2.2 Comparison of wearable ECG monitoring systems.

Ref.	Device name (Year)	Strain reduction from sensors	Continuous data transmission	Level of activities	Substrate	Electrode type	Electrode reusability
This work	SIS (2021)	Yes (strain isolator)	> 8 hours* (single device)	Real, continuous daily activities, including excessive jogging	Perforated, breathable silicone	Dry	Yes
[19]	MAX-ECG (commercial)	No	48 hours** (with a battery replacement)	-	Adhesive patch	Wet	No
[45]	Zio (commercial)	No	No***	-	Adhesive patch	Wet	No
[21]	CAM (commercial)	No	No***	-	Adhesive patch	Wet	No
[22]	Cardiostat (commercial)	No	No***	-	Gel electrode	Wet	No
[46]	No name (2019)	No	< 1 hour (not portable)	In-lab activities	Acrylic adhesive	Wet	No
[18]	No name (2019)	No	< 1 hour (with a chest strap)	In-lab activities	Elastic strap	Wet	No
[40]	No name (2019)	No	3 hours	Simulated in-lab sitting/standing	Silicone elastomer	Dry	Yes
[44]	SEP (2019)	No	< 1 hour (with a wired circuit)	Simulated in-lab jogging	Silicone elastomer	Dry	Yes

* Sample rate: 256 Hz.
** Sample rate: 128 Hz.
*** Data saving to a local storage, not for real-time, continuous data transmission.

CHAPTER 3. SYSTEM OVERVIEW

The device developed in this study is referred to as a strain isolated soft bioelectronics (SIS). Figure 3.1 summarizes the design overview of an SIS, structure layouts, strain-isolation mechanics, and the device functions. The all-in-one, soft, imperceptible system has an exceptionally small form factor (Figure 3.1A) that adheres securely and discretely to the chest area for continuous health and motion monitoring throughout various daily activities. The schematic illustration in Figure 3.1B shows the multi-layered device structure, including a pair of skin-mounted sensors, strain-isolating blocks, soft elastomeric membranes, printed circuit board (PCB), and integrated chip components. Thus, the SIS's most crucial component is a pair of strain-isolating layers (SIL) in Figure 3.1B. The SIL is positioned above each electrode. Among the components, a pair of nanomembrane mesh electrodes makes direct contact with the skin for measuring non-invasive physiological signals, such as ECG, heartrate (HR), and respiration rate (RR) This open-mesh, stretchable electrode can endure excessive tensile strain up to 100% without failure. The SIS's bottom layer is an extremely low modulus silicone gel with excellent adhesive properties to bond the device to the skin. The top layer is a low modulus silicone elastomer that provides a durable platform to mount the circuit and makes the device more comfortable to handle and prevents unwanted sticking to clothes. The miniaturized PCB and rechargeable battery are secured and encapsulated with the silicone elastomer. The circuit is mounted in the center on a thin layer of silicone gel to allow a greater range of bending without skin delamination.

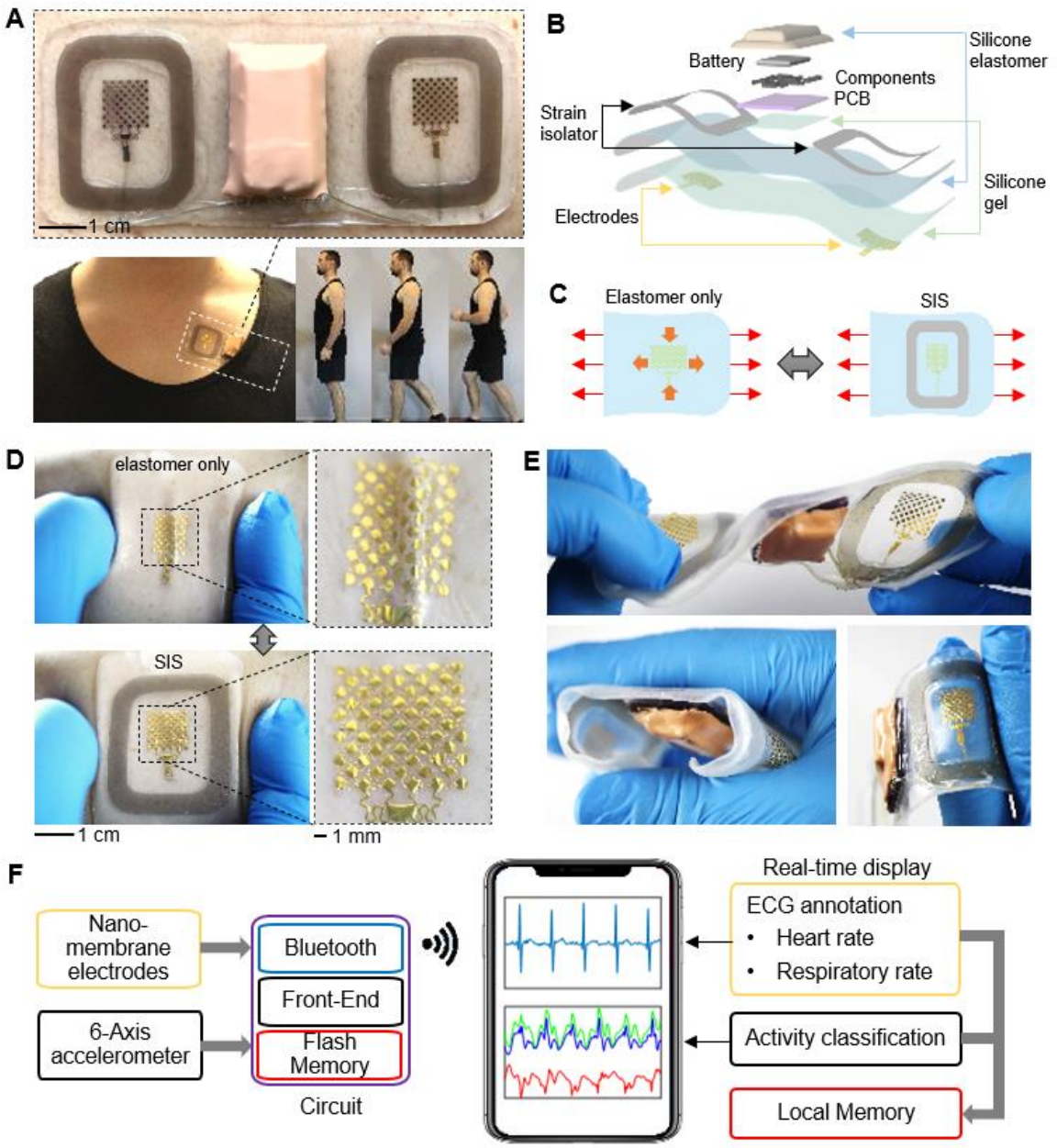

Figure 3.1 Overview of the SIS

The unique feature of this design is the SIL mounted above each electrode. Figure 3.1C visualizes the deformation the substrate and electrodes would exhibit under uniaxial strain. Typically, MA to the wearable device on the chest area arises from typical daily activities, such as standing, walking, running, or sudden arm movements. In various movement

conditions, the SIL in the SIS device surrounds and shields the electrodes from excessive or sudden strain while leaving the elastomer directly over the electrodes free to maintain conformal contact at the skin-electrode interface. Photos in Figure 3.1D capture how the SIL can offer strain isolation for the electrode, directing skin strain to areas less critical to signal quality. The entire device, including all necessary components and a rechargeable battery, still maintains mechanical flexibility and stretchability. As shown in Figure 3.1E, the SIS is capable of twisting, bending, and stretching, beyond the expected deformation of intended application sites on the upper torso. The schematic illustration in Figure 3.1F describes the data processing workflow of the SIS and signal monitoring/storage via a portable smart device. The measured data from the electrodes and the onboard accelerometer are transmitted via Bluetooth to the user's smartphone or tablet for real-time display or recording of physiological signals. A custom-designed Android application can display real-time ECG data, 3-axis angular orientation data, and 3-axis acceleration. Further ECG annotation and long-term health data can be calculated at the end of each session. While some device designs presented by other groups aim to reduce strain at the electrodes using stiff adhesive patches or fabric backings[18, 19], they result in increased stiffness and rigidity of the device, losing the conformal electrode contact to the skin as well as consistent signal quality. On the other hand, the presented SIS maintains the quality of skin-electrode contact with a soft elastomeric membrane, while limiting the excessive strain transmission to the electrode via the SIL integration. Thus, the SIS can offer continuous, high-quality health monitoring in real-life activities at homes or clinical settings.

CHAPTER 4. MATERIALS AND METHODS

4.1 Materials

4.1.1 SIS Assembly

Device assembly, depicted in the top of Figure 4.1 as a simplified side view of the device, starts with the two layer elastomer substrate. The circuit is attached with an additional layer of silicone gel. The strain isolation layers are attached directly to the top of the substrate with a thin layer of silicone adhesive. The electrodes are placed on the bottom of the substrate using water soluble tape. The electrodes are then connected to the circuit with flexible thin film connections. The battery and circuit are encapsulated with elastomer to prevent tugging at connections, and to waterproof the electrical components.

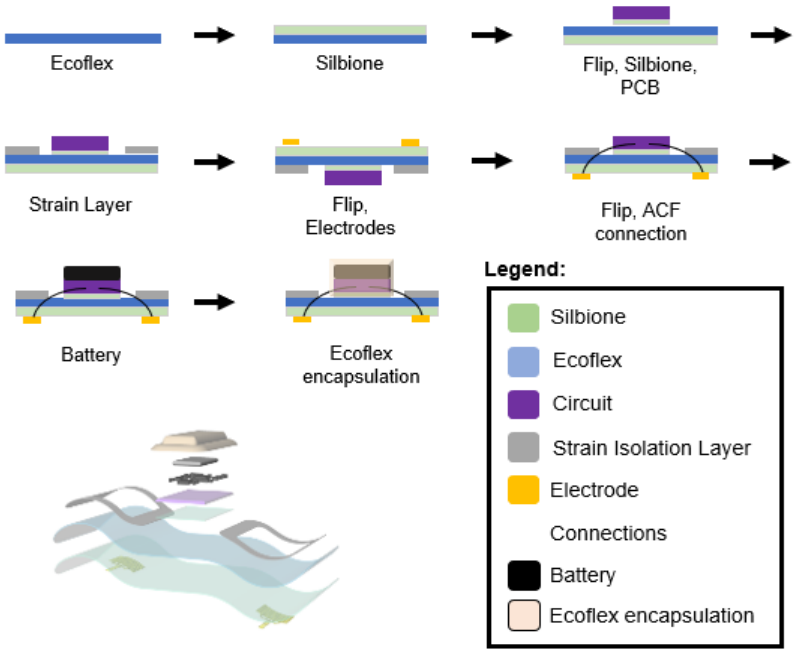

Figure 4.1 SIS assembly steps

4.1.2 Elastomer Substrate Fabrication

A custom mold was fabricated in four sequential steps shown in Figure 4.2A from left to right. First, an array of holes was laser cut in 3 mm acrylic sheet. A reverse mold was cast using DragonSkin™ (Smooth-On) to produce a flexible array of needles, followed by another DragonSkin™ mold to produce a flexible array of holes. Finally, EpoxAcast™ 670 HT (Smooth-On) was cast, producing a needle array of 3 mm tall, tapered needles spaced 1.5 mm apart (Figure 4.2B). Each molding step was preceded by applying generous mold release for easy removal, and the material was only allowed to cure after using a vacuum chamber to evacuate trapped air. Epoxy needles with a base diameter less than 0.5 mm were prone to breaking during elastomer removal. Perforated breathable substrates were produced by pouring elastomer layers into the epoxy mold (Figure 4.2C). Since the perforations are shaped by the tapered needles with a larger diameter base, the silbione layer was applied first for a larger diameter hole facing the skin (Figure 4.2D). This encouraged the outward wicking of moisture from the skin. The silbione was spin-coated at 800 rpm for 60 s and allowed to cure for 24 hours. Next, Ecoflex 30 was spin-coated at 200 rpm for 30 s and allowed to cure for 5 hours. Final perforated substrates were carefully removed from the mold for thin-film integration with the circuit and electrodes using a similar assembly process as smooth substrates. Total substrate thickness was 1.5-2.0 mm, while thinner samples were difficult to remove from the mold without tearing.

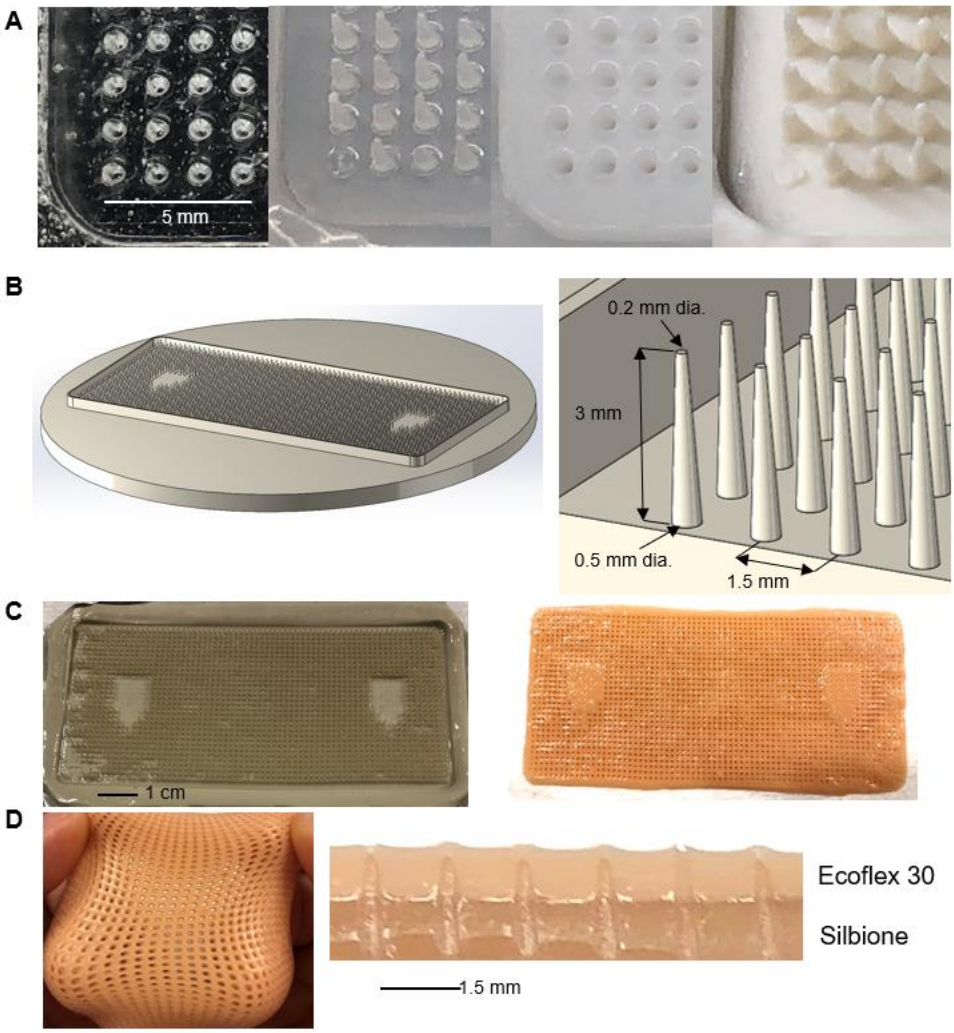

Figure 4.2 Breathable substrate fabrication

4.1.3 Electrode Fabrication

The thin, nanofilm mesh electrodes are fabricated by standard photolithography and metal etching in a micro-electronics cleanroom. Figure 4.3 shows the sequence, starting from the top left. A silicon wafer is coated with Polydimethylsiloxane (PDMS) as a release layer. Polyimide (PI) is coated before Chromium and Gold deposition. A series of photoresist (PR) patterning and metal etching steps produce the electrode patterned

electrode, which is further encapsulated with PI to reenforce and insulate the electrode. PI etching is done using reactive ion plasma etching to reveal the gold electrode contact pads.

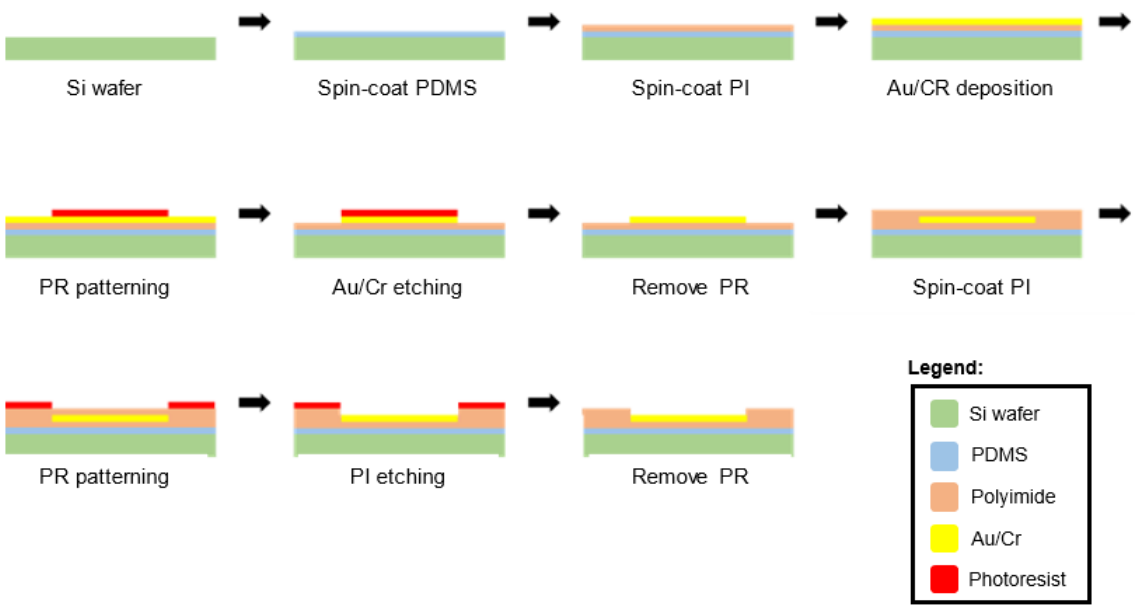

Figure 4.3 Electrode fabrication

4.2 Strain Isolation

4.2.1 Contact Impedance

The change in contact impedance was measured for gel and dry electrodes to quantify how much change occurs when different components are disturbed. The testing was conducted on the forearm with wires connecting the electrodes to a B&K LCR meter. Figure 4.4A shows the three types of disturbance: shaking wires, direct pressure on the electrode, and pressure on the skin immediately surrounding the electrode. The peak-to-peak change of each portion of time was normalized with respect to the initial impedance value for each category with the resulting bar graph in Figure 4.4B. The results of gel electrodes are shown in Figure 4.4C and the sharp changes in amplitude from 50-100 s

indicate that direct pressure makes an immediate change to the impedance. This contrasts with the skin disturbance for gel electrodes, which was close to that of the wires. The dry electrode test, shown in Figure 4.4D, has similar results for wires, but a very different waveform for electrode and skin. There is an initial decrease near 50 s when pressure was placed on the electrode, but this established a new contact impedance that remained for the duration of the test. The following disturbance to the electrode and skin are much more similar, and even their values in the bar graph are close. This discover led to further investigation as to why these disturbances were similar, which is further modeled in the next section.

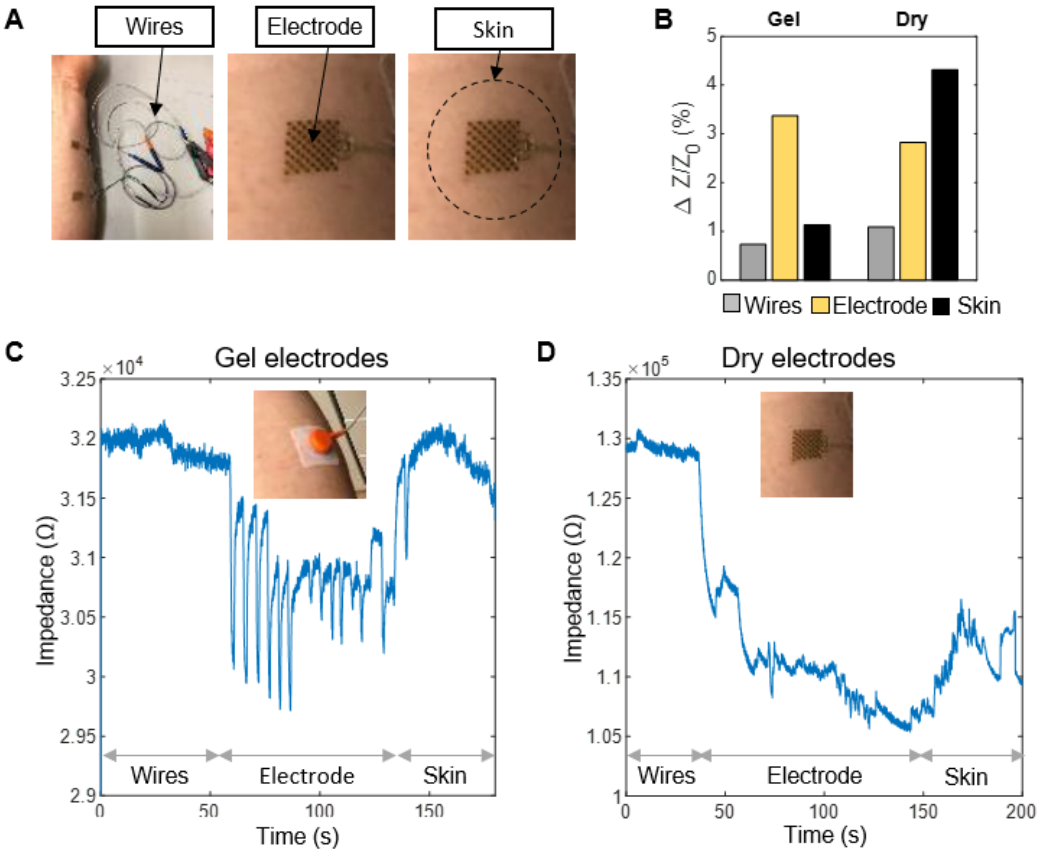

Figure 4.4 Sources of impedance change

4.2.2 Skin Strain Model

A circular electrode and skin are in unstrained steady-state configuration (Figure 4.5A) and the skin under biaxial strain (Figure 4.5B) with stretch ratios λ_1, λ_2. The area of skin in contact with the electrode remains the same. When the skin experiences strain, the electrode moves with the skin, but remains relatively unstrained. This loading scenario causes a portion of the skin that is initially in contact with the electrode to slide out of contact with the electrode. If the skin strain is held constant, then a new steady-state will be reached at the current skin/electrode interface. One source of MA is caused by the impedance change that occurs when the skin moves relative to the electrode. The sensitivity of the skin/electrode interface is quantified by the change in the area in contact at the skin/electrode interface, depicted as the gray ellipse in B. The stretch ratio is defined as

$$\lambda_i = \frac{L + \delta_i}{L} = 1 + \varepsilon_i \qquad i = 1,2 \tag{1}$$

where L is the original length, δ_i is the elongation, and ε_i is the strain. Equation (1) can be rearranged to describe the new length as

$$\lambda_i L = L + \delta_i \qquad i = 1,2 \tag{2}$$

From Figure 4.5B, it can be shown that the stretch ratios also define the new half lengths

$$a = \lambda_1 r, \;\; b = \lambda_2 r. \tag{3}$$

The change in area is calculated using the area of an ellipse minus the area of the circular electrode

$$\delta A = \pi ab - \pi r^2. \tag{4}$$

Substituting a, b from (3) into (4) results in

$$\delta A = \pi r^2(\lambda_1 \lambda_2 - 1). \tag{5}$$

Mesh electrodes (Figure 4.5C) can be modeled as an N numbered array of small electrodes with a radius r_1, having a total area equal to a single electrode with radius r_2, the relationship given by

$$\mathrm{A} = \pi N r_1^2 = \pi r_2^2. \tag{6}$$

After substituting the area from (6) into (5), we can show that the change in area is directly proportional to the stretch ratios for a single electrode or an array of electrodes by

$$\delta A = A(\lambda_1\lambda_2 - 1) = \pi N r_1^2(\lambda_1\lambda_2 - 1) = \pi r_2^2(\lambda_1\lambda_2 - 1). \tag{7}$$

Therefore, the total change in area for an array is proportional to the strain across the entire array, regardless of the radius of each individual pad.

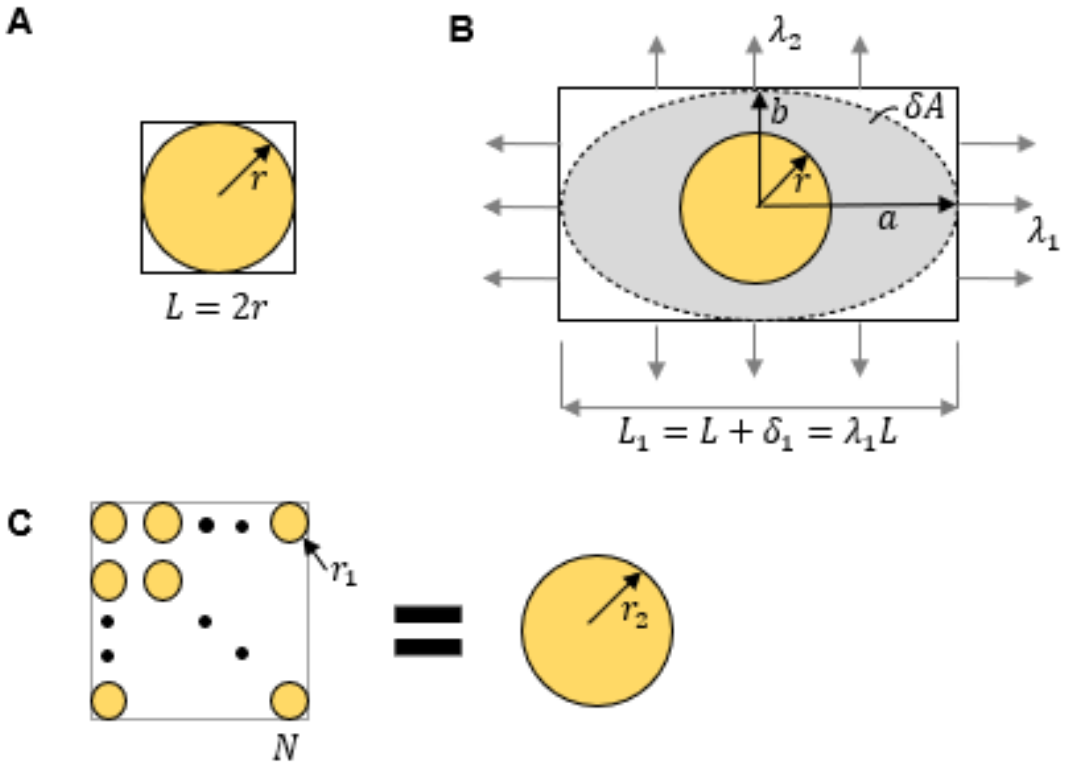

Figure 4.5 Skin strain model

4.2.3 Strain Layer Material Characterization

The strain layer was cut from solid sheets of polypropylene. Various lengths of material were cut and subjected to a bending test (Figure 4.6A) to determine Young's modulus for accurate modeling of stiffness. For a sheet modeled as a cantilever beam fixed at one end, the deflection from a force at the tip is calculated by[47]

$$\delta = \frac{PL^3}{3EI} \tag{8}$$

where δ is the deflection at the free end, P is the force, L is the beam length, E is Young's modulus, and I is the moment of inertia of a rectangular beam (Figure 4.7B). From this equation, the modulus can be calculated by

$$E = \left(\frac{P}{\delta}\right)\frac{4L^3}{bh^3} \tag{9}$$

where $\left(\frac{P}{\delta}\right)$ is the measured value from the bending test and determined by a linear least-squares fit of the data. The data from each trial was trimmed to exclude inertia effects of the measurement device near the ends of travel, shown in Figure 4.6B. The Young's modulus was calculated after conversion of the force data using the sample dimensions (Figure 4.6C) and averaged over three trials using samples of different lengths and slightly different widths. The SIL sheet thickness h for all samples is 0.31 mm, along with the base width (b) = 29.35, 28.78, 28.37 mm, and the length (L) = 18.0, 20.7, 23.2 mm.

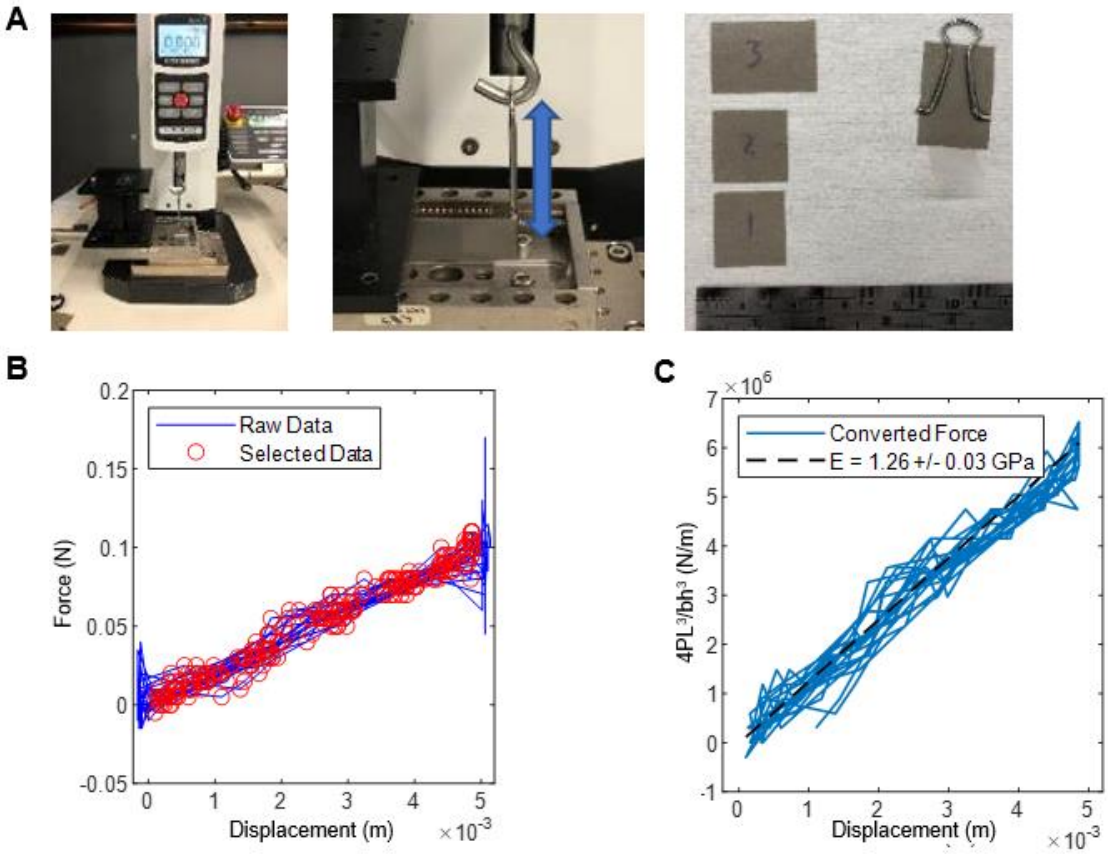

Figure 4.6 Strain layer material characterization

4.2.4 Strain Layer Development

Strain layer geometry was developed based on the given electrode dimensions. Using principal mechanics equations[47], the minimum and maximum thickness were derived to minimize in-plane-strain while allowing for expected out-of-plane bending to maintain conformal contact with the skin. First, the elongation value of the middle section (Figure 4.7A) was calculated for the sheet modeled as a prismatic beam, given by

$$\delta = \frac{PL}{EA} \tag{10}$$

where A is the cross-sectional area for a rectangular beam. The two edge portions are modeled as a simply supported beam with point load and maximum deflection in the middle given by

$$\delta = \frac{PL^3}{48EI}. \tag{11}$$

Together, the elongation from (10) and bending of the edges from (11) add up to the total strain inside the perimeter of the SIL. Combining these equations and solving for h results in

$$h_{min} = \frac{PL}{2Eb\delta_{allow}}\left(1 + \frac{L^2}{12b^2}\right). \tag{12}$$

where h_{min} is the minimum sheet thickness required to keep the elongation below δ_{allow}. Actual values are $\mathrm{P} = 1\,N$, $L = 21\,mm$, $E = 1.22\,GPa$, $\mathrm{w} = 5.5\,mm$, and $\delta_{allow} = 0.64\,mm$ based on 2% strain of the inner dimension L. Resulting in $h_{min} = 14.2\,\mu m$.

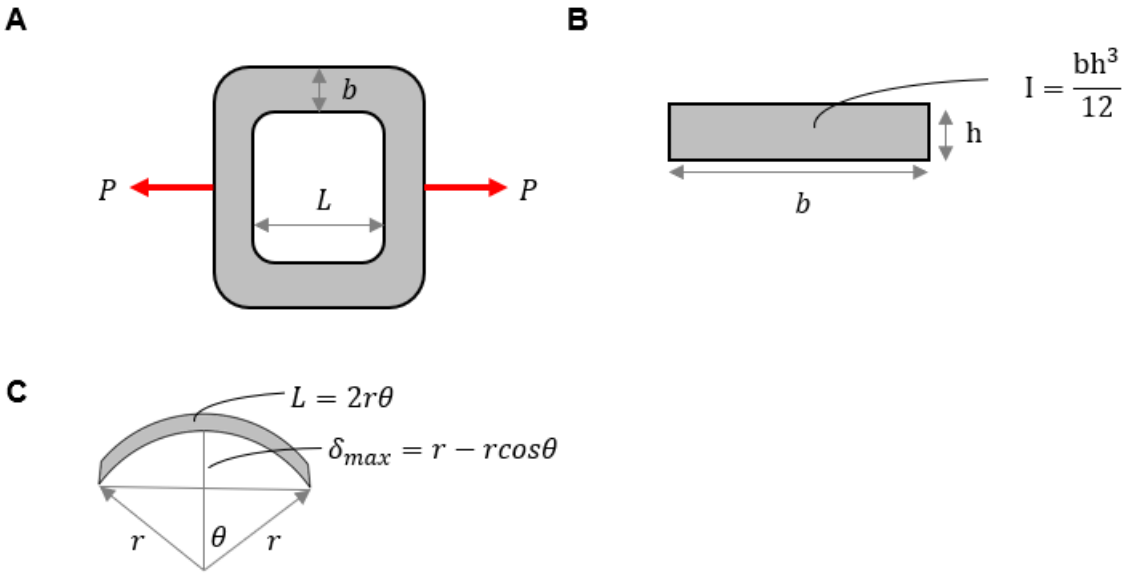

Figure 4.7 Schematic of strain isolation layer

4.3 Finite Element Analysis

Commercial software ABAQUS was used to validate analytical calculations and optimize mechanical performance. The three main components considered were the elastomer substrate, the PCB circuit, and the strain isolation layer, with the mesh, loading conditions and preliminary strain results shown in Figure 4.8. All components were meshed using hexahedral elements: elastomer (C3D8RH), PCB circuit (C3D8), and strain isolation layer (C3D8R), with 787 total elements and 1876 total nodes. The elastomer substrate was modeled as a hyperelastic Neo-Hooke material with coefficients $D_1 = 10.152$, $\mathrm{C}_{10} = 4.8E-02$. The elastic modulus ($E$) and Poisson's ratio ($\nu$) are $E_{PCB} = 24$ GPa, $\nu_{PCB} = 0.12$, $E_{SIL} = 1.22$ GPa, $\nu_{SIL} = 0.43$.

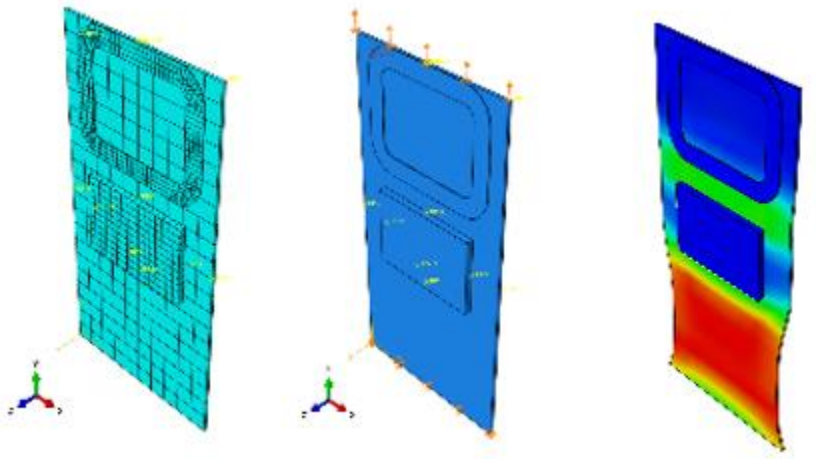

Figure 4.8 FEA mesh and loading conditions

4.4 Signal Processing

The signal-to-noise ratio (SNR) is used to assess the signal quality and quantify the motion artifacts. SNR calculation was made by identifying the heartrate peaks using a

variation of the Pan-Tompkins algorithm for detecting the QRS complex[48]. Figure 4.9 shows the sequence starting in the top left. First, the raw signal is filtered using a 0.5-30 Hz bandpass filter to eliminate baseline wander and other high frequency noise such as powerline interference. A derivative filter and squaring of the values accentuate the absolute values of all peaks. A convolutional filter combines the absolute value of the two adjacent peaks from each QRS complex resulting in a relative amplitude used here as the signal. These signal peaks were removed using a high-order median filter (order = 99), leaving the remaining noise. The signal-to-noise ratio was then calculated using

$$SNR_{dB} = 10\log_{10}\frac{A_{signal}}{A_{noise}} \tag{13}$$

as the ratio of the average amplitude of each QRS complex versus the average noise amplitude.

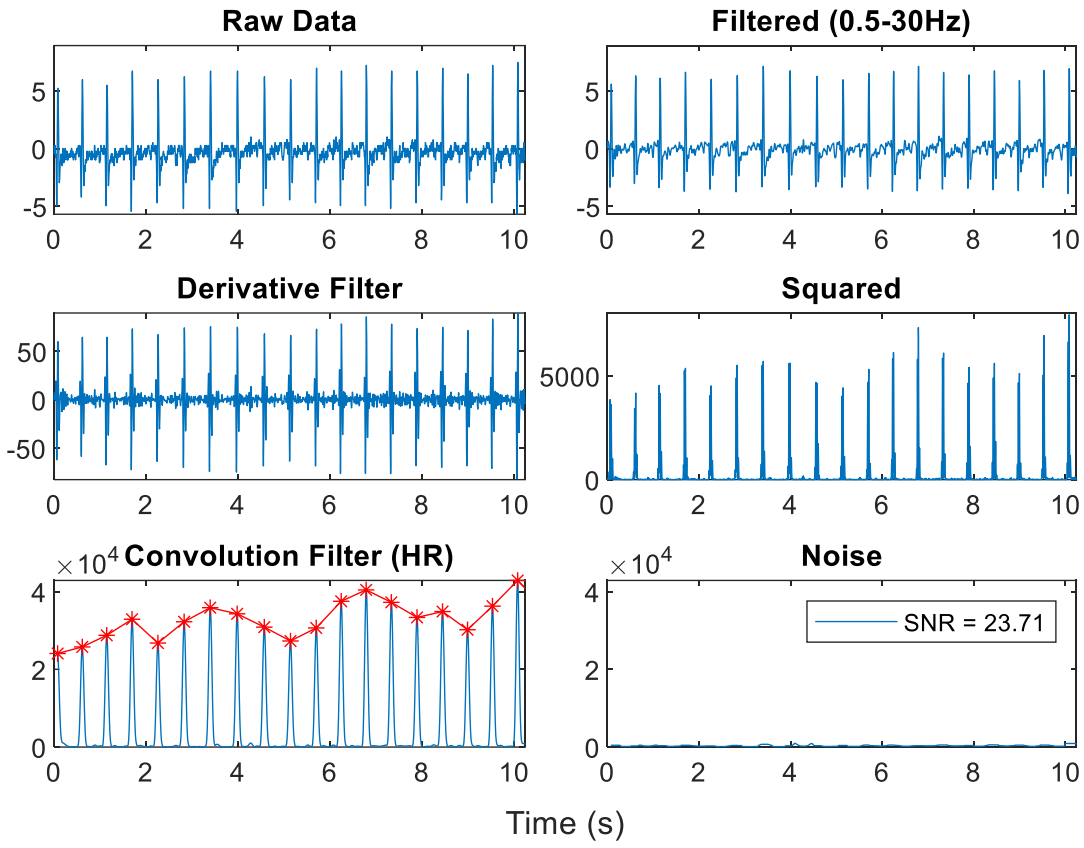

Figure 4.9 ECG signal filtering and SNR calculation

CHAPTER 5. RESULTS AND DISCUSSION

5.1 Material Results

5.1.1 Adhesion

Conformal contact and secure adhesion are critical for high signal quality. The adhesive value of the elastomer substrates were tested using a peel test on the forearm. Figure 5.1A shows the device with the stain layer removed. Peel tests of the SIS with and without the strain layer produced similar results, but the strain layer showed an increased adhesive value. The plot in Figure 5.1B shows the adhesive peel force with the corresponding part of the device superimposed above. There is a clear rise in peel force from 10-30 mm followed by a decrease after the circuit has peeled up from the skin. This was visually observed during the test. Next, the test with the strain layer shows a similar feature, where the average peel force is 0.2614 N/cm compared to 0.1832 N/cm for the elastomer alone. The strain layer surrounds the electrode and distributes the upward force over a larger area of elastomer. This is similar to the way in which a Command™ hook (3M) has good adhesion when the hook is in place, but to remove the adhesive one only needs to pull down on the strip with much less force than what the hook can withstand. This is an added benefit of strain isolation that helps secure the electrode from external force.

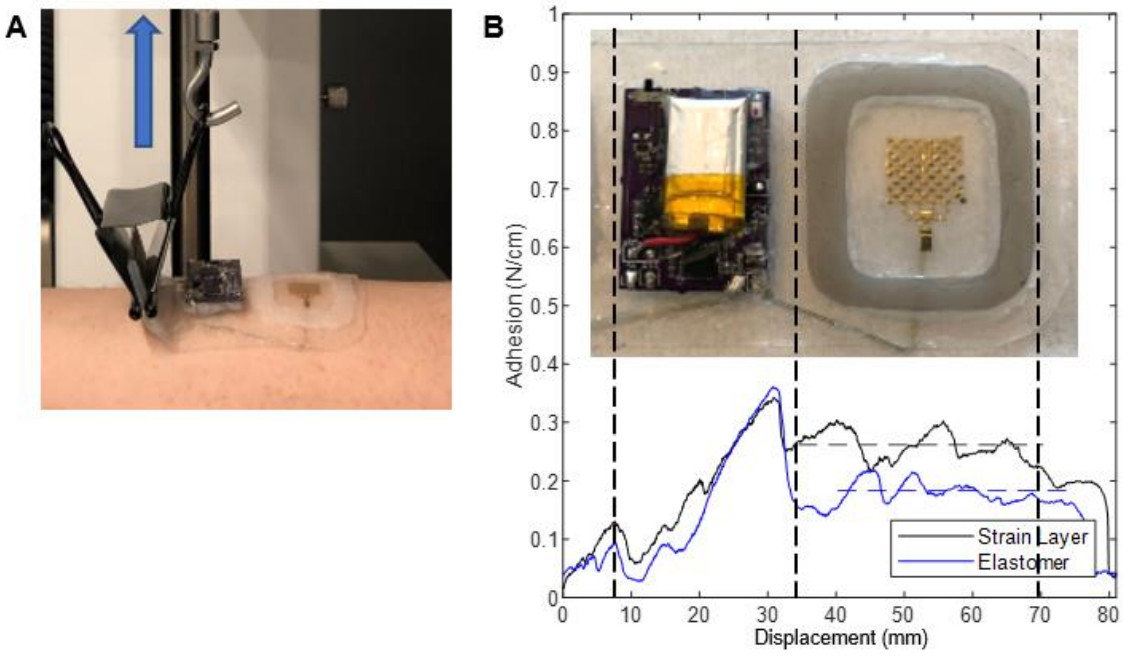

Figure 5.1 Results of adhesion peel test

5.1.2 Breathability

The need for a breathable device became clear while testing motion artifacts for jogging during the summer. Acceptable signal quality would soon give way to huge motion artifacts and finally complete delamination of the device. The breathable fabrication detailed in section 4.1.2 produced substrates capable wicking sweat away to maintain adhesion and a stable signal amplitude. Samples of different elastomer materials, thicknesses and perforation patterns were tested following guidelines from ASTM E 96. Glass jars were filled with distilled water and sealed with the samples. The jars were placed in a temperature-controlled oven and measured for change in mass at regular intervals. The samples were rotated into a new position following each measurement to reduce the possibility of uneven evaporation between samples. Two tests were conducted, the first (Figure 5.2A) also included the widely used commercially available and breathable

medical adhesive Tegaderm (3M), shown as sample number 4. The second test (Figure 5.2B) included the final version of the Silbione and Ecoflex substrate with electrodes and strain layers blocking some of the perforations to test the breathability at the electrode, shown as sample number 11.

The water vapor transmission rate is a measure of the mass able to flow through the substrate. This value will change for a material depending on environmental factors. The temperature and humidity were different between the two tests, but each sample was also normalized by percentages of their respective open samples, jar 1 and jar 7. Sample 11 had a value of 13.24% whereas the Tegaderm sample 4 had a value of 8.17%. Other comparisons between samples that were repeated in both tests confirm that the comparison is valid. Samples 2 and 8, as well as samples 6 and 12 used the same elastomer and have very similar percentages despite their different water vapor transmission values.

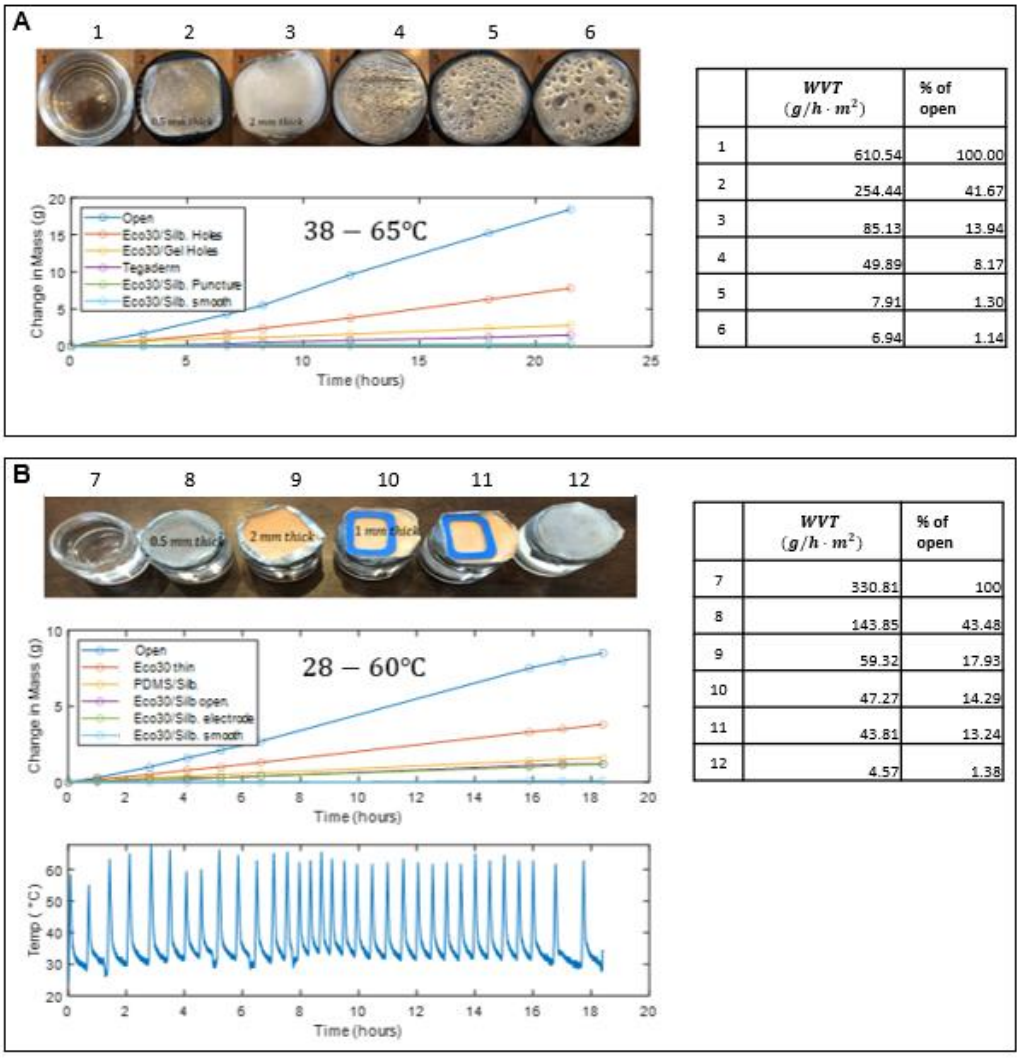

	WVT $(g/h \cdot m^2)$	% of open
1	610.54	100.00
2	254.44	41.67
3	85.13	13.94
4	49.89	8.17
5	7.91	1.30
6	6.94	1.14

	WVT $(g/h \cdot m^2)$	% of open
7	330.81	100
8	143.85	43.48
9	59.32	17.93
10	47.27	14.29
11	43.81	13.24
12	4.57	1.38

Figure 5.2 Results of water vapor transmission test with breathable elastomer

5.1.3 Strain Reduction

The collected data in Figure 5.3 shows the finite element analysis (FEA) result of a device with the applied tensile strain (15%) in the vertical direction to mimic a stretched human skin. The bottom electrode, without the integrated SIL, experiences 36% strain, while the top electrode that is shielded by the SIL has a calculated strain of 3%. The change in contact area for each electrode is proportional to strain, meaning that the total area of skin sliding past each tiny electrode pad on the bottom electrode is over 12 times the change

occurring in the top electrode. It is clear that less change occurs with the top electrode protected by the SIL.

The second noteworthy observation is that the device is still able to withstand the elongation. The areas in between the SIL and circuit stretch well within the limits of their elastic range. The idea of tuned stiffness or hard-soft integration is used in other fields, and has benefit for wearable electronics. Restricting some skin strain, while allowing other areas to flex and move means that portions of the device can maintain good adhesion and contact, while the forces spread across the entire device still have some areas to deform.

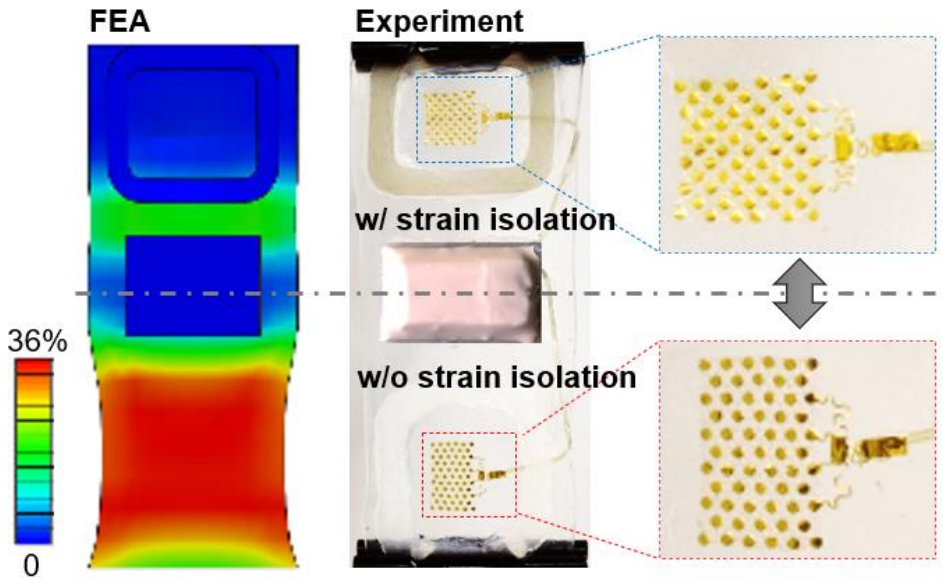

Figure 5.3 FEA and experimental results of axial strain test

5.2 ECG Results of SIS

5.2.1 Comparison with Identical Electrodes

To evaluate the performance of the SIL, short and repeatable comparison tests were conducted with a stopwatch on an indoor course. Each three-minute trial consisted of 30-

second intervals for each activity in the following order: idle (0 mph), walking (2 mph), fast walking (4 mph), jogging (6 mph), walking (2 mph), and idle (0 mph). The same device was used for eight total trials, four of which occurred before the SIL was mounted to a bare elastomer substrate, and four trials were conducted with the SIL-integrated device. Consistent skin preparation and device placement were carefully repeated, and the device was removed after each trial to demonstrate the electrode's reusability. The summarized results from Figure 5.4A show representative data; an SIS shows a clear reduction of MA compared to a bare elastomer case without the SIL material. The corresponding data are shown in Figure 5.4F where the signal to noise ratio (SNR) is calculated from all trials (n=4). Although both cases show decreased SNR during jogging, the SIS maintains better signal quality than the elastomer-only case. The mean SNR reduction from idle to jog was 31.6 to 16.9 dB for elastomer compared to 30.3 to 22.0 dB for the SIL; this is a reduction of signal quality by 47% for elastomer alone versus 27% for the SIS when compared to their respective baseline idle signals.

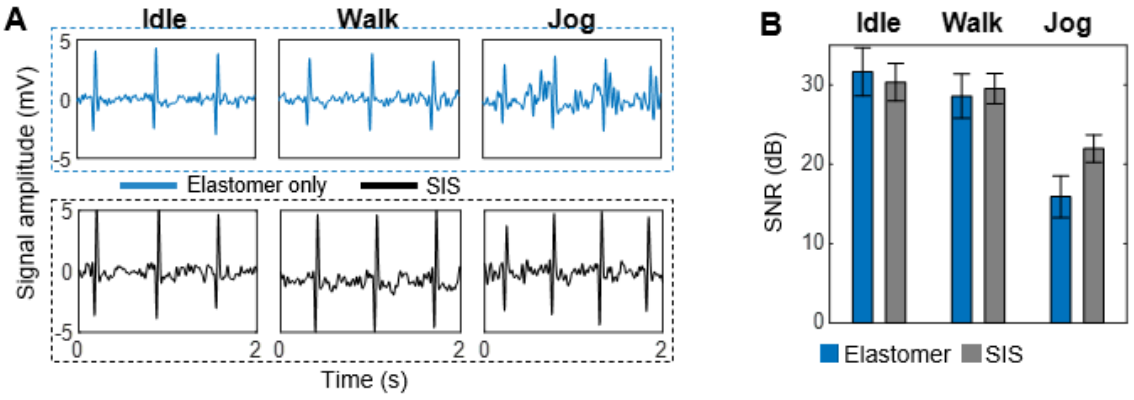

Figure 5.4 Results of jogging test with SIS compared to no strain isolation

5.2.2 Comparison with Commercial Device

To validate the device performance, the SIS was worn with another commercial wireless heart monitor for simultaneous ECG recording on the chest area. Photos in Figure 5.5A show an SIS and a commercial all-in-one device (MAX-ECG Monitor, Maxim Integrated, Inc.) on the chest. Although both devices have a similar footprint, the commercial one contains a stiffer fabric-backed adhesive gel electrode patch shown to buckle and delaminate from the skin. The strain experienced across the entire length of the patch becomes concentrated at the edge where the circuit is connected, resulting in delamination directly over the electrode. This observation highlights the SIS's advantage of tuned stiffness specifically at the electrode, while still allowing the rest of the device to have conformal contact to the skin that can endure body movements. Figure 5.5B plots the SNR results from four simultaneous tests of the two devices, with mean idle values normalized for comparison. The mean SNR reduction from idle to jog was 25.7 to 12.1 dB for the commercial device compared to 25.7 to 21.6 dB for the SIS. This is a reduction of signal quality by 53% for the commercial device versus 16% for the SIS when compared to their respective baseline idle signals. Raw ECG plots in Figure 5.5C show 2-second comparisons for idle, walk, and jog from one trial, capturing increased MA as a user's activity level increases. On the other hand, the SIS could maintain the signal quality levels. The normalized ECG amplitudes are shown for equal comparison, to compensate for the smaller signal in the commercial device partially due to its placement higher on the chest, and thereby, farther from the heart. A more extended trial with additional exercises is shown in Figure 5.5D. The moving average HR calculations show a slight increase during walking and jogging (30-150 s), followed by a slight decrease during resting (150-200 s)

before rising higher for the remaining exercises (200-350 s). Both devices plot a similar trend throughout the test until the burpee exercise (300 s) introduces over 5-g acceleration. The SIS shows a noticeable jagged deviation indicating MA interfering with the HR algorithm, but the plot continues smoothly after the exercise is finished. Unlike the SIS, the amplitude of MA from the commercial one significantly interferes with the HR algorithm, resulting in a complete failure in HR and RR detection after 300 s (Figure 5.5D). Throughout the testing session, the commercial device has higher fluctuation in the detection of continuous HR and RR than the SIS. In a similar way, we compared the effect of arm movements to the wearable devices. Plots in Figure 5.5E summarize the measured ECG data from the SIS and the MAX-ECG when a subject has constant arm movements, capturing significant MA from the commercial device.

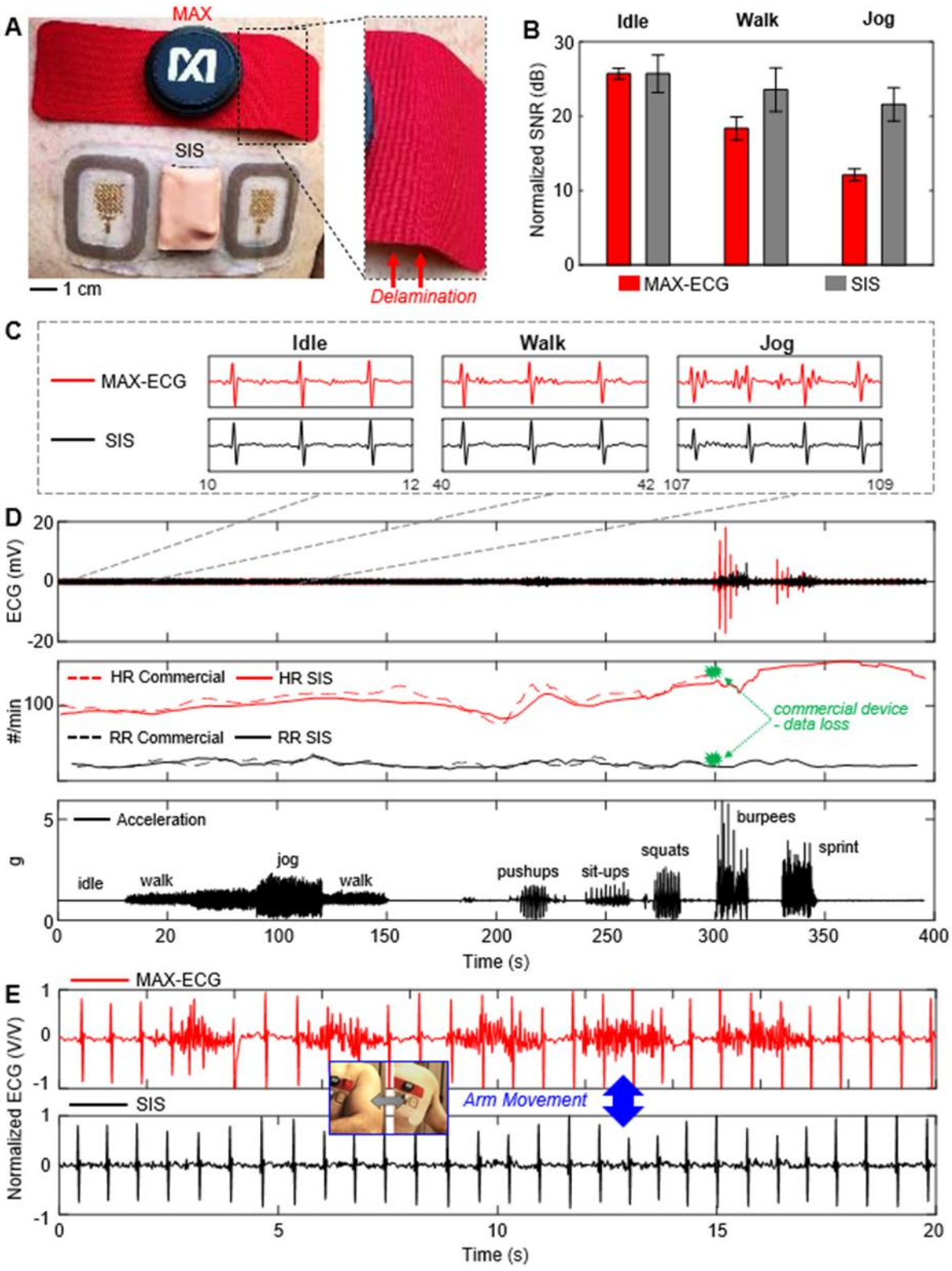

Figure 5.5 Results of simultaneous testing of SIS and commercial device

5.2.3 Validation of Long-term Monitoring

Further testing was conducted to evaluate the SIS's long-term performance for everyday use and real-life activities. The testing protocol involved normal daily activities such as rest, deskwork, household chores, and exercises (Figure 5.6A). Participants were instructed to wear the device under comfortable clothes and follow a schedule that included activities from each category. A representative set of recorded data in Figure 5.6B shows an example of real-time, continuous recording of physiological data for 8-consecutive hours: raw ECG data with user-reported activities of four different colors (top), measured HR and RR data from ECG, showing clear signals even with excessive motions (middle). The acceleration data is classified by intensity level throughout the recording to give an overall measure of activity throughout the day and daily totals of these four types of activities (idle, walk, fast walk, and jog). HR and RR are continuously monitored throughout the day and activity classification without any MA issues or device delamination problems.

A comparison plot in Figure 5.6C shows the percentage of time spent in each of the four types of activities. It compares the reported time by a participant with the calculated time measured by the activity classification. There are apparent discrepancies in the reported times by the user report and classified one. In general, participants underestimated time spent in the two lowest activity categories while overestimated time spent in the two higher activity categories. Since activity level is used to give a better picture of overall health, having quantifiable measurements can help, especially with the tendency to overestimate the healthy choices we are making.

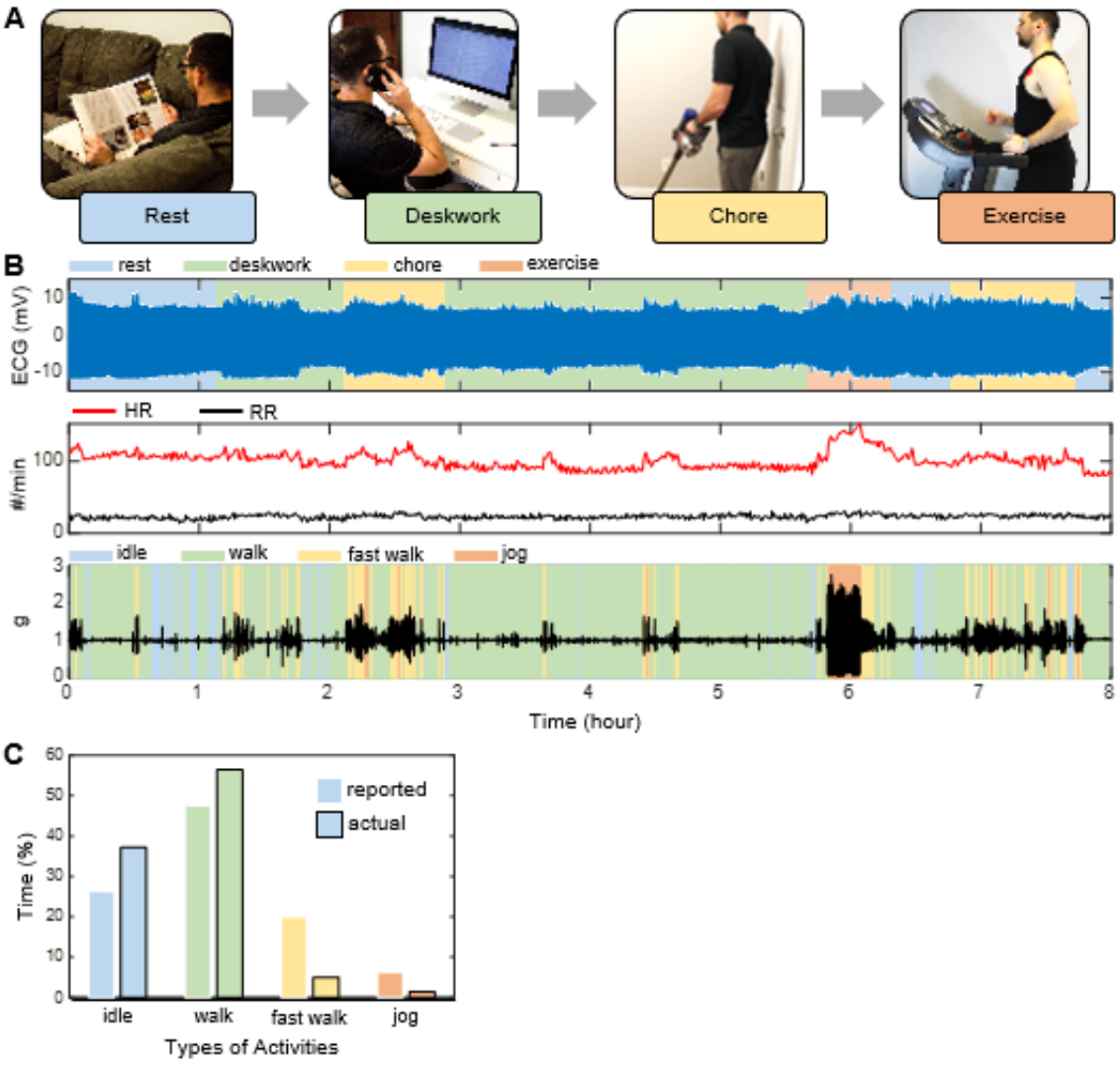

Figure 5.6 Results of 8-hour ECG measurement with multiple activities

CHAPTER 6. CONCLUSION AND FUTURE WORK

6.1 Conclusion

This work presented a description of ECG measurement, a definition of motion artifacts, and a review of wearable ECG devices and their limitations. The SIS device has been presented as a capable solution to wireless ECG monitoring. Details of the fabrication and methods for developing the device have also been presented. The skin strain model for correlating strain and motion artifacts as well as the development of strain isolation for mesh electrodes were described. Results confirmed the importance of adhesion and breathability for consistent signal quality. Signal to noise ratio was used to compare signal quality between tests and between devices. Stain isolation resulted in better signals that with identical electrodes without strain isolation. The SIS showed a marked improvement over a comparable commercial device in multiple tests and was able to continuously monitor ECG signals throughout daily activities, including exercise.

6.2 Future Work

The strain isolation concept has potential to be used in other wearable electronics. Relative motion and skin strain cause motion artifacts for other signals such as photoplethysmogram (PPG), electroencephalogram (EEG), electromyogram (EMG), etc. There may also be commercial applications for strain isolation with gel electrodes or wire restraints to improve quality in the clinic as well.

REFERENCES

[1] "Wearable Technology Market Size Worth $104.39 Billion By 2027," ed, 2020.

[2] "Wearable Health Technologies And Their Impact On The Health Industry," ed, 2019.

[3] "Wearables Are Totally Failing the People Who Need Them Most," ed.

[4] E. J. Benjamin *et al.*, "Heart Disease and Stroke Statistics-2019 Update: A Report From the American Heart Association," *Circulation,* vol. 139, no. 10, pp. e56-e528, 2019, doi: 10.1161/CIR.0000000000000659.

[5] J. Heikenfeld *et al.*, "Wearable sensors: Modalities, challenges, and prospects," vol. 18, ed: Royal Society of Chemistry, 2018, pp. 217-248.

[6] M. Alghatrif and J. Lindsay, "A brief review: history to understand fundamentals of electrocardiography," *Journal of Community Hospital Internal Medicine Perspectives,* vol. 2, no. 1, p. 14383, 2012, doi: 10.3402/jchimp.v2i1.14383.

[7] "Anatomy and Function of the Heart's Electrical System," ed. Johns Hopkins Medicine.

[8] W. Einthoven, "Ueber die Form des menschlichen Electrocardiogramms," *Pflüger, Archiv für die Gesammte Physiologie des Menschen und der Thiere,* vol. 60, no. 3-4, pp. 101-123, 1895, doi: 10.1007/bf01662582.

[9] "artifact," in *The American Heritage® Medical Dictionary*, ed: Houghton Mifflin Company, 2007.

[10] Z. Zhang, I. Silva, D. Wu, J. Zheng, H. Wu, and W. Wang, "Adaptive motion artefact reduction in respiration and ECG signals for wearable healthcare monitoring systems," *Medical and Biological Engineering and Computing,* vol. 52, no. 12, pp. 1019-1030, 2014, doi: 10.1007/s11517-014-1201-7.

[11] M. Kirst, B. Glauner, and J. Ottenbacher, "Using DWT for ECG motion artifact reduction with noise-correlating signals," *Proceedings of the Annual International Conference of the IEEE Engineering in Medicine and Biology Society, EMBS,* pp. 4804-4807, 2011, doi: 10.1109/IEMBS.2011.6091190.

[12] G. FERRI, V. STORNELLI, and A. D. SIMONE, "A CCII-BASED HIGH IMPEDANCE INPUT STAGE FOR BIOMEDICAL APPLICATIONS," *Journal of Circuits, Systems and Computers,* vol. 20, no. 08, pp. 1441-1447, 2011, doi: 10.1142/s021812661100802x.

[13] G. Bortolan, I. Christov, I. Simova, and I. Dotsinsky, "Noise processing in exercise ECG stress test for the analysis and the clinical characterization of QRS and T wave alternans," *Biomedical Signal Processing and Control,* vol. 18, pp. 378-385, 2015, doi: 10.1016/j.bspc.2015.02.003.

[14] Y. Liu and M. G. Pecht, "Reduction of Skin Stretch Induced Motion Artifacts in Electrocardiogram Monitoring Using Adaptive Filtering," 2006.

[15] A. Kalra and A. Lowe, "Development and validation of Motion Artefact Rejection System (MARS) for electrocardiography using novel skin-stretch estimation approach," *Sensors and Actuators, A: Physical,* vol. 301, pp. 111726-111726, 2020, doi: 10.1016/j.sna.2019.111726.

[16] H. Zhang and J. Zhao, "Motion artefact suppression method for wearable ECGs," *Feature Engineering and Computational Intelligence in ECG Monitoring,* pp. 73-88, 2020, doi: 10.1007/978-981-15-3824-7_5.

[17] S. C. Lee and S. M. Kim, "Motion artifact reduction algorithm in wearable healthcare system," *Journal of Medical Devices, Transactions of the ASME,* vol. 10, no. 2, 2016, doi: 10.1115/1.4033169.

[18] B. Porr and L. Howell, "R-peak detector stress test with a new noisy ECG database reveals significant performance differences amongst popular detectors," pp. 1-27, 2019, doi: 10.1101/722397.

[19] "MAX-ECG-MONITOR User Guide," 2018.

[20] P. M. Barrett *et al.*, "Comparison of 24-hour Holter monitoring with 14-day novel adhesive patch electrocardiographic monitoring," *American Journal of Medicine,* vol. 127, no. 1, pp. 95.e11-95.e17, 2014, doi: 10.1016/j.amjmed.2013.10.003.

[21] R. Rho, M. Vossler, S. Blancher, and J. E. Poole, "Comparison of 2 ambulatory patch ECG monitors: The benefit of the P-wave and signal clarity," *American Heart Journal,* vol. 203, pp. 109-117, 2018.

[22] I. Nault *et al.*, "Validation of a novel single lead ambulatory ECG monitor - Cardiostat - Compared to a standard ECG Holter monitoring," *J Electrocardiol,* vol. 53, pp. 57-63, Mar - Apr 2019, doi: 10.1016/j.jelectrocard.2018.12.011.

[23] S. Upadhyayula and R. Kasliwal, "Wellysis S-PAtch Cardio versus Conventional Holter Ambulatory Electrocardiographic Monitoring (The PACER Trial): Preliminary Results," *Journal of Clinical and Preventive Cardiology,* vol. 8, no. 4, pp. 173-173, 2019, doi: 10.4103/jcpc.jcpc_43_19.

[24] J. A. Walsh, E. J. Topol, and S. R. Steinhubl, "Novel wireless devices for cardiac monitoring," *Circulation,* vol. 130, no. 7, pp. 573-581, 2014, doi: 10.1161/CIRCULATIONAHA.114.009024.

[25] R. Herbert, J.-H. Kim, Y. S. Kim, H. M. Lee, and W.-H. Yeo, "Soft material-enabled, flexible hybrid electronics for medicine, healthcare, and human-machine interfaces," *Materials,* vol. 11, no. 2, p. 187, 2018.

[26] H. R. Lim, H. S. Kim, R. Qazi, Y. T. Kwon, J. W. Jeong, and W. H. Yeo, "Advanced soft materials, sensor integrations, and applications of wearable flexible hybrid electronics in healthcare, energy, and environment," *Advanced Materials,* vol. 32, no. 15, p. 1901924, 2020.

[27] Y. Fu, J. Zhao, Y. Dong, and X. Wang, "Dry Electrodes for Human Bioelectrical Signal Monitoring," *Sensors (Basel),* vol. 20, no. 13, Jun 29 2020, doi: 10.3390/s20133651.

[28] J. Ottenbacher, M. Kirst, L. Jatobá, M. Huflejt, U. Großmann, and W. Stork, "Reliable motion artifact detection for ECG monitoring systems with dry electrodes," *Proceedings of the 30th Annual International Conference of the IEEE Engineering in Medicine and Biology Society, EMBS'08 - "Personalized Healthcare through Technology",* pp. 1695-1698, 2008, doi: 10.1109/iembs.2008.4649502.

[29] Y. M. Chi, T. P. Jung, and G. Cauwenberghs, "Dry-contact and noncontact biopotential electrodes: Methodological review," *IEEE Reviews in Biomedical Engineering,* vol. 3, pp. 106-119, 2010, doi: 10.1109/RBME.2010.2084078.

[30] J. W. Jeong *et al.*, "Materials and optimized designs for human-machine interfaces via epidermal electronics," *Advanced Materials,* vol. 25, no. 47, pp. 6839-6846, 2013, doi: 10.1002/adma.201301921.

[31] Y.-T. Kwon *et al.*, "All-printed nanomembrane wireless bioelectronics using a biocompatible solderable graphene for multimodal human-machine interfaces," *Nature communications,* vol. 11, no. 1, pp. 1-11, 2020.

[32] H. Kim *et al.*, "Fully Integrated, Stretchable, Wireless Skin-Conformal Bioelectronics for Continuous Stress Monitoring in Daily Life," *Advanced Science,* vol. 7, no. 15, p. 2000810, 2020.

[33] L. Tian *et al.*, "Large-area MRI-compatible epidermal electronic interfaces for prosthetic control and cognitive monitoring," *Nature Biomedical Engineering,* vol. 3, no. 3, pp. 194-205, 2019/03/01 2019, doi: 10.1038/s41551-019-0347-x.

[34] E. Huigen, A. Peper, and C. A. Grimbergen, "Investigation into the origin of the noise of surface electrodes," 2002, vol. 40. [Online]. Available: www.biosemi.com

[35] X. An and G. K. Stylios, "A hybrid textile electrode for electrocardiogram (ECG) measurement and motion tracking," *Materials,* vol. 11, no. 10, p. 1887, 2018.

[36] N. T. Tasneem, S. A. Pullano, C. D. Critello, A. S. Fiorillo, and I. Mahbub, "A low-power on-chip ecg monitoring system based on mwcnt/pdms dry electrodes," *IEEE Sensors Journal,* vol. 20, no. 21, pp. 12799-12806, 2020.

[37] H. U. Chung *et al.*, "Skin-interfaced biosensors for advanced wireless physiological monitoring in neonatal and pediatric intensive-care units," *Nature Medicine,* vol. 26, no. 3, pp. 418-429, 2020, doi: 10.1038/s41591-020-0792-9.

[38] H. U. Chung *et al.*, "Binodal, wireless epidermal electronic systems with in-sensor analytics for neonatal intensive care," *Science,* vol. 363, no. 6430, pp. 0-13, 2019, doi: 10.1126/science.aau0780.

[39] Y.-S. Kim *et al.*, "All-in-One, Wireless, Stretchable Hybrid Electronics for Smart, Connected, and Ambulatory Physiological Monitoring," *Advanced Science,* vol. 6, no. 17, 2019, doi: 10.1002/advs.201900939.

[40] R. Lin, Y. Li, X. Mao, W. Zhou, and R. Liu, "Hybrid 3D Printing All-in-One Heterogenous Rigidity Assemblies for Soft Electronics," *Advanced Materials Technologies,* vol. 4, no. 12, pp. 1-8, 2019, doi: 10.1002/admt.201900614.

[41] Y. Liu *et al.*, "Intraoperative monitoring of neuromuscular function with soft, skin-mounted wireless devices," *npj Digital Medicine,* vol. 1, no. 1, 2018, doi: 10.1038/s41746-018-0023-7.

[42] M. Zulqarnain *et al.*, "A flexible ECG patch compatible with NFC RF communication," *npj Flexible Electronics,* vol. 4, no. 1, pp. 1-9, 2020, doi: 10.1038/s41528-020-0077-x.

[43] W. Dong, X. Cheng, T. Xiong, and X. Wang, "Stretchable bio-potential electrode with self-similar serpentine structure for continuous, long-term, stable ECG recordings," *Biomedical Microdevices,* vol. 21, no. 1, 2019, doi: 10.1007/s10544-018-0353-x.

[44] Y. Li *et al.*, "A Stretchable-Hybrid Low-Power Monolithic ECG Patch with Microfluidic Liquid-Metal Interconnects and Stretchable Carbon-Black Nanocomposite Electrodes for Wearable Heart Monitoring," *Advanced Electronic Materials,* vol. 5, no. 2, pp. 1-12, 2019, doi: 10.1002/aelm.201800463.

[45] E. Fung *et al.*, "Electrocardiographic patch devices and contemporary wireless cardiac monitoring," *Frontiers in Physiology,* vol. 6, no. MAY, 2015, doi: 10.3389/fphys.2015.00149.

[46] D. Berwal, C. R. Vandana, S. Dewan, C. V. Jiji, and M. S. Baghini, "Motion Artifact Removal in Ambulatory ECG Signal for Heart Rate Variability Analysis," *IEEE Sensors Journal,* vol. 19, no. 24, pp. 12432-12442, 2019, doi: 10.1109/JSEN.2019.2939391.

[47] B. J. Goodno and J. M. Gere, *Mechanics of materials*, Ninth Edition / ed. Australia: Cengage Learning, 2018, pp. xxiv, 1159 pages.

[48] W. J. Tompkins and J. Pan, "A Real-Time QRS Detection Algorithm," 1985, vol. 32.